International Journal of Naval Architecture and Ocean Engineering 14 (2022) 100434

Contents lists available at ScienceDirect

International Journal of Naval Architecture and Ocean Engineering

journal homepage: http://www.journals.elsevier.com/international-journal-of-naval-architecture-and-ocean-engineering/

Development and verification of modeling practice for numerical estimation of wind loads on offshore floating structures

Seong Mo Yeon [a, *], Erwan Auburtin [b], Zhirong Shen [c], Sebastien Loubeyre [d], Byung Hyuk Lee [e], Min-Guk Seo [a], Lucia Sileo [f], Hyun Joe Kim [g]

[a] Korea Research Institute of Ships and Ocean Engineering (KRISO), Daejeon, Republic of Korea
[b] Technip Energies, Paris La Défense, France
[c] American Bureau of Shipping, Houston, USA
[d] Bureau Veritas Solutions Marine and Offshore, Nantes, France
[e] Korea Shipping and Offshore Engineering, Ulsan, Republic of Korea
[f] SINTEF Ocean, Trondheim, Norway
[g] Samsung Heavy Industries, Daejeon, Republic of Korea

ARTICLE INFO

Article history:
Received 11 July 2021
Received in revised form
22 December 2021
Accepted 26 December 2021
Available online 1 January 2022

Keywords:
CFD
Wind loads
ABL
STAR-CCM+
OpenFOAM
Semi-submersible rig
FPSO
Modeling practice

ABSTRACT

Mean wind load on a semi-submersible rig and an FPSO was investigated by using Computational Fluid Dynamics (CFD) for the modeling practice developed in Reproducible Offshore CFD JIP. The modeling practice is benchmarked against available model test results for a semi-submersible rig and an FPSO in blind manner between verifiers. For the semi-submersible rig, an even keel and four inclined conditions were considered. The uncertainty levels between verifiers' results were within 10%. Slightly larger scatter was observed in inclined conditions but did not show any larger than 10% uncertainty level. It was possible to reduce the discrepancy by easing the setting difference from the wind tunnel test by introducing gap around deckbox and columns. For the FPSO, the results were within 3% for forces and within 14% for moments. After considering model test setup including the gap between FPSO hull bottom and turntable, the results were improved and within 10% error between the results and wind tunnel test except for 120 and 240° headings.

© 2022 Society of Naval Architects of Korea. Production and hosting by Elsevier B.V. This is an open access article under the CC BY license (http://creativecommons.org/licenses/by/4.0/).

1. Introduction

Mean wind load is one of the major design loads for the hull and mooring of offshore floating structures, especially owing to much larger projected area above water than under water. It is customary that a wind tunnel test is carried out based on the wind speed for model test condition instead of the design wind speed. The wind speed for model test is determined through the Reynolds number dependency test instead of applying the Reynolds' law of similarity to the design wind speed in full scale considering the capacity of wind tunnel facilities because the fully turbulent flow assumption can be justified and the aerodynamic characteristics of the flow remain almost plateaued at Re = 10^7 and above (Roshko, 1961; Achenbach, 1968), in which the design wind speed is determined. In this regard, more emphasis is placed on the wind profile shape.

There were many studies to implement wind profile shape in numerical way, especially sustainable wind profile. Richards and Hoxey (1993) was the first to implement successfully neutral stratified Atmospheric Boundary Layer (ABL) below Ekman layer. They showed that ABL can be an analytic solution of the Navier-Stokes equations with the assumption of steady-state, horizontally homogeneous wind profile and high Re and derived boundary conditions referred to as RH conditions which make both wind profile and turbulence quantities retainable and sustainable throughout the computational domain. Sumner and Masson (2010) and Richards and Norris (2011) investigated overshoot issue of turbulent kinetic energy near the ground and identified the main cause was due to the inconsistency of discretization while applying RH conditions. Kim et al. (2018) suggested an alternative and practical way to diminish the overshoot issue without modifying

* Corresponding author.
E-mail address: seongmo.yeon@kriso.re.kr (S.M. Yeon).
Peer review under responsibility of The Society of Naval Architects of Korea.

https://doi.org/10.1016/j.ijnaoe.2021.100434
2092-6782/© 2022 Society of Naval Architects of Korea. Production and hosting by Elsevier B.V. This is an open access article under the CC BY license (http://creativecommons.org/licenses/by/4.0/).

Nomenclature

λ	Scale ratio
ν	Kinematic viscosity of air
ω	Specific dissipation rate
ρ	Density of air
z_0	Roughness length
U_{ref}	Reference speed at the reference height
u_*	Friction velocity
U_{target}	Target wind speed which could be either model test condition or design speed in full scale
ϵ	Turbulent dissipation rate
y^+	Dimensionless wall distance
z_{ref}	Reference height
B	Breadth
C_k	Non-dimensional coefficient for M_x defined as $C_k = \frac{M_x}{0.5\rho L_{pp}^3 U_{\text{target}}^2}$
C_m	Non-dimensional coefficient for M_y defined as $C_m = \frac{M_y}{0.5\rho L_{pp}^3 U_{\text{target}}^2}$
C_n	Non-dimensional coefficient for M_z defined as $C_n = \frac{M_z}{0.5\rho L_{pp}^3 U_{\text{target}}^2}$
C_x	Non-dimensional coefficient for F_x defined as $C_x = \frac{F_x}{0.5\rho L_{pp}^2 U_{\text{target}}^2}$
C_y	Non-dimensional coefficient for F_y defined as $C_y = \frac{F_y}{0.5\rho L_{pp}^2 U_{\text{target}}^2}$
C_z	Non-dimensional coefficient for F_z defined as $C_z = \frac{F_z}{0.5\rho L_{pp}^2 U_{\text{target}}^2}$
E_r	Relative Error defined as $E_r = \frac{\text{Solution}^{\text{fine}} - \text{Solution}^{\text{coarse}}}{\text{Solution}^{\text{coarse}}}$
F_x	Force in x direction
F_y	Force in y direction
F_z	Force in z direction
H	Hieght from keel
k	Turbulent kinetic energy
L_{pp}	Length between perpendiculars
M_x	Moment around x direction
M_y	Moment around y direction
M_z	Moment around z direction
R	Convergence Ratio
Re	Reynolds number defined as $Re = \frac{UL_{pp}}{\nu}$
T	Draft
U	Wind speed
U_F	Uncertainty for forces
U_M	Uncertainty for moments

discretization such that turbulent kinetic energy near bottom can have more sustainable form.

With recent advancements in numerical schemes used in Computational Fluid Dynamics (CFD), the offshore industry has begun using CFD as an alternative tool to compute wind loads on offshore floating structures including semi-submersibles and FPSOs (Kim et al., 2018, 2019; Yeon et al., 2019; Xu et al., 2019; Koop et al., 2012). In order to promote CFD as an acceptable tool comparable to wind tunnel tests, efforts were made in the Reproducible Offshore CFD JIP to develop a practical CFD modeling practice. In the JIP, verifiers were required to build a CFD model including meshes and set up a sustainable wind profile for their favorite CFD solvers including Siemens STAR-CCM+ and OpenFOAM with a developed modeling document shared.

In this paper, an overview of the developed modeling practice and the CFD results from verifiers in blind tests are provided. The modeling practice is based on the work of TESK JDP (Yeon et al., 2019) and further refined for benchmarking against available model test results for a semi-submersible rig and an FPSO. In general, wind tunnel models are tend to be fabricated with wind tunnel's own practice. Especially, structures like truss and wired mesh may not follow the dimensions in CAD drawing in order to reflect aerodynamic characteristics in full scale. CFD model also can be modified and simplified in order to facilitate mesh generation and avoid degenerate mesh by eliminating insignificant small objects. In the study, however, CFD model and wind tunnel model were forced to be derived from one source of CAD model without modification such that CFD model and wind tunnel model were generated in model-to-model basis in order to minimize geometric uncertainty.

2. Sustainable wind profile modeling

2.1. Wind profile

The mean wind speed profile from NPD (Norwegian Petroleum Directorate) (Andersen and Løvseth, 2006; API, 2000) is expressed by

$$U(z) = U_{\text{ref}}\left(1 + A\ln\frac{z}{z_{\text{ref}}}\right) \tag{1}$$

where $A = 0.057\,3\sqrt{1 + 0.15U_{\text{ref}}}$, U_{ref} is the reference speed at the reference height, z_{ref}, which is normally 10 m above the still water.

The NPD profile comprises two parts: scaling factor U_{ref} and profile shape $(1 + A\ln\frac{z}{z_{\text{ref}}})$. Since the profile shape is a function of dimensional wind speed as well as non-dimensional elevation, the profile shape is not consistent and has different forms between model scale and prototype in comparison with API profile. To resolve the issue of having different forms depending on scale ratio, SNAME−OC−8 (Kim et al., 2018, 2019) proposed the following form which is used in this study:

$$U(z) = U_{\text{target}}\left(1 + A\ln\frac{z}{z_{\text{ref}}}\right) \tag{2}$$

where U_{target} is the wind speed either for model or for prototype depending on the scale ratio and U_{ref} is the wind speed for prototype.

2.2. Auxiliary conditions for sustainability

In order to enforce sustainable wind profile with turbulence properties, turbulent quantities should be imposed along with the NPD profile as follows (Kim et al., 2018, 2019; Yeon et al., 2019):

For $k-\omega$ model,

$$\begin{aligned} k(z) &= \frac{u_*^2}{\sqrt{\beta_*}} \\ \omega(z) &= \frac{u_*}{\kappa\sqrt{\beta_*}(z + z_0)} \end{aligned} \tag{3}$$

For $k-\epsilon$ model

$$k(z) = \frac{u_*^2}{\sqrt{C_\mu}}$$
$$\epsilon(z) = \frac{u_*^3}{\kappa(z+z_0)} \quad (4)$$

where friction velocity and roughness length are defined as follows:

$$u_* = \kappa A U_{\text{target}}$$
$$z_0 = z_{\text{ref}} Exp\left[-\frac{1}{A}\right] \quad (5)$$

Further detailed setup for sustainable wind profile are referred to Yeon et al. (2019).

3. Computational setup

3.1. Coordinate system and heading convention

The coordinate system is defined as shown in Fig. 1. Positive x, y and z are in the bow, port and opposite to the gravity directions, respectively. The origin is located at the midship on the water surface.

Heading angles are defined following the OCIMF convention (OCIMF, 1994) such that angles are shown from 0° at the stern to 180° bow in counter-clockwise direction.

For Semi-submersible rigs, overturning moments are one of primary quantities of interest and described in critical wind direction and critical axis as shown in Fig. 2. The critical axis is defined as a line perpendicular to the critical wind direction in which the greatest overturning moment for the models on an even keel is obtained. Inclined condition is defined around the critical axis.

3.2. Computational domain and boundary conditions

Fig. 3 shows the computational domain for the CFD simulations. L_x is the longitudinal length, L_y is the width, and L_z is the height of the domain. The computational domain is decided in terms of characteristic length L and H. L is defined as the maximum width of the deckbox for the semi-submersible rig and distance between perpendiculars (L_{pp}) for the FPSO. H is the height of the hull including tower structures like the derrick boom or the flare tower.

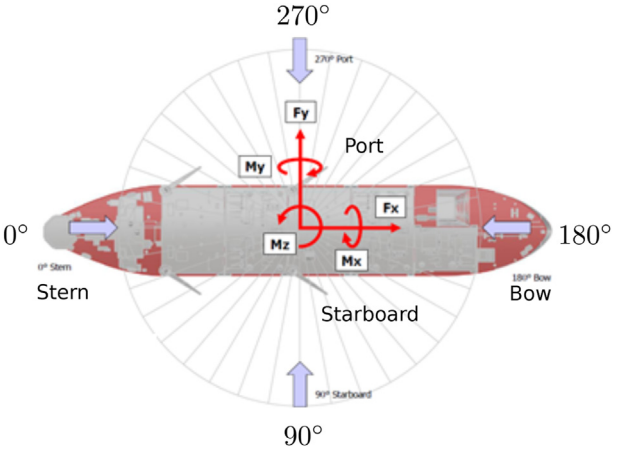

Fig. 1. Horizontal coordinate system.

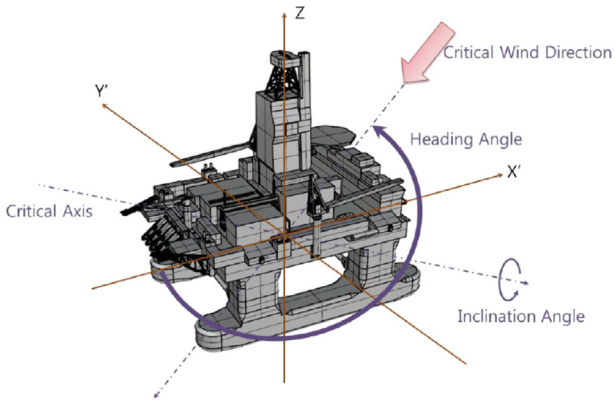

Fig. 2. Critical axis for inclined conditions.

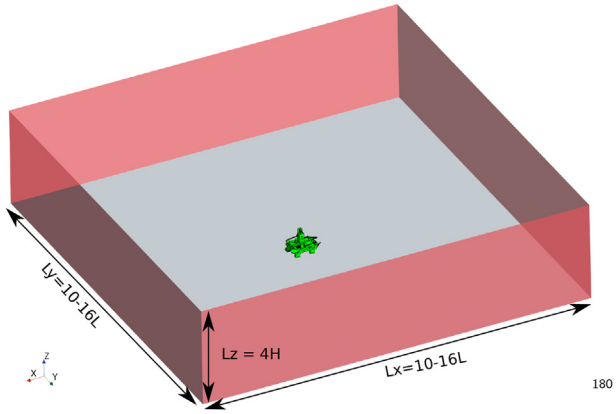

Fig. 3. Computational domain.

The horizontal domain is defined as a rectangular shape with a minimum size of 10L in order to consider heading changes. The height of the domain is defined as 4H.

As shown in Fig. 4, the boundary conditions are velocity inlet at the flow inlet, top and the two lateral sides, pressure outlet at the flow outlet, no-slip condition of smooth wall on the hull. Bottom boundary which represents the still water level is given a no-slip condition with rough wall for the sustainable wind profile (Kim et al., 2018, 2019; Yeon et al., 2019).

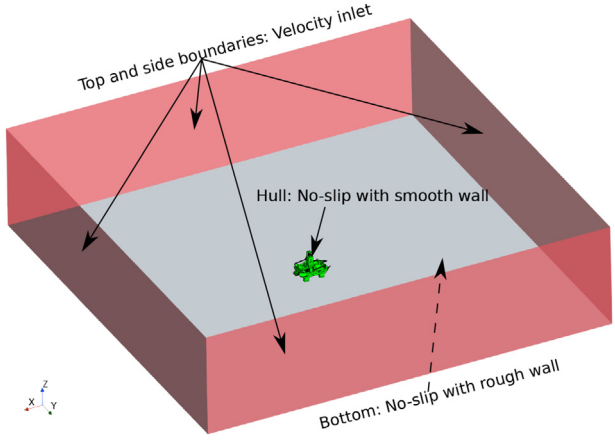

Fig. 4. Boundary conditions.

3.3. Volumetric mesh

Unstructured hexahedral grids are used for volume mesh. Several refinement zones are introduced to capture flow structures in wakes properly as shown in Fig. 5. Grid size for the volumetric refinement zones are parameterized in terms of characteristic length L. For the semi-submersible rig, the grid sizes for the zones are 2%L, 4%L and 8%L, respectively. For the FPSO, the grid sizes are 0.5%L, 1%L and 2%L, respectively.

Prism layer mesh can be used to resolve boundary layer flow near the hull. However, it was found that the prism layers did not show significant difference in predicted wind loads during the TESK JDP (Yeon et al., 2019). Thus, the use of prism layer may not be considered a critical issue for the wind load simulation in both the semi and FPSO cases.

3.4. Numerical setup

Based on lessons learned from TESK JDP (Yeon et al., 2019) in which unsteady analysis including DES simulation showed a difference of only 3% in mean drag forces compared to the RANS steady-state analysis, steady-state calculations were conducted for incompressible flow from a practical point of view. For steady simulations, at least 2000 iterations are performed to obtain the mean wind load coefficnets from the converged solutions.

The numerical setups are summarized in Table 1. For a general-purpose commercial software, Siemens STAR-CCM+, segregated incompressible solver was applied. Hybrid Gauss-Least Square Method was used for gradient calculation as the discretization scheme and upwind scheme was used for the convection terms. For an open source software, OpenFOAM(Weller et al., 1998), segregated incompressible solver was applied. LeastSquares scheme was used for gradient calculation as the discretization scheme and linearUpwindV scheme for momentum equations and upwind scheme for others was used for the convection terms.

3.5. Turbulence model

Following Eqs. (3) and (4), $k-\epsilon$ and $k-\omega$ models are applicable to the modeling of the sustainable wind profile. During the benchmark, realizable $k-\epsilon$ and $k-\omega$ SST models were chosen and showed little difference on the estimated wind load. For simplicity, only results by $k-\omega$ SST are presented.

4. Wind load study

4.1. Grid sensitivity study

Grid sensitivity study for $k-\omega$ SST turbulence model was carried out with three different meshes for the FPSO described in section 4.4: coarse, medium and fine meshes. Three different heading angles, 90, 150 and 180 were chosen according to the heading convention shown in Fig. 1. The grid sensitivity were studied with the non-dimensional wind load coefficients C_x and C_y and the results are summarized in Table 2. Since it could be seen that the solutions were converged after 1000 iterations, total iterations were set to at least 2000 iterations as shown in Fig. 6. The mean wind load coefficients were obtained by using the last one third iterations.

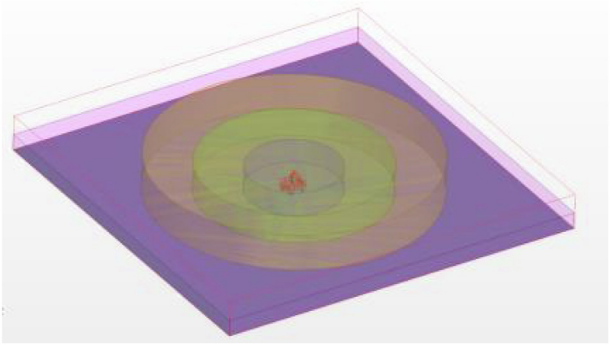

Fig. 5. Volume refinement.

Table 1
Numerical setup.

	STAR-CCM+	OpenFOAM
solver	Segrigated	segrigated
gradient	Hybrid Gauss-Least Square	leastSquares
convection	Upwind	linearUpwindV upwind

In the study, air density $\rho = 1.21$ kg/m$^{\circ}$ and $U_{\text{ref}} = 40$ m/s and $U_{\text{target}} = 19.1$ m/s were used, respectively. Convergence ratio R (Xing and Stern, 2010) was used to determine the convergence condition, which is defined as follows:

$$\begin{aligned} S &= \frac{\varepsilon_{21}}{\varepsilon_{32}} \\ \varepsilon_{21} &= \text{Solution}_{\text{medium}} - \text{Solution}_{\text{fine}} \\ \varepsilon_{32} &= \text{Solution}_{\text{coarse}} - \text{Solution}_{\text{medium}} \end{aligned} \tag{6}$$

For the C_x, R values showed negative values which mean oscillatory convergence. For the C_y, monotonic convergence behavior was observed at 150 heading angle and oscillatory convergence behavior was observed at 90 heading angle. The grid sensitivity study showed convergence behavior. In terms of relative error E_r, E_r between the medium and fine meshes showed much smaller values, at most less than around 5% than E_r between coarse and medium meshes. From the practical point of view, medium mesh would be sufficient for the subsequent simulations for the semi-submersible rig and FPSO. For benchmark, all the verifiers were advised to make meshes in the range of 30–40 million cells.

4.2. Wind profile

Before applying to wind load estimation, the retainability of wind profile imposed at the boundaries throughout the computational domain or the sustainability of the wind profile was examined between verifiers in a blind manner. For simplicity, wind profiles measured in the middle of the domain were plotted with the wind profile (NPD) imposed at the boundaries and the wind tunnel data (EFD) as in Fig. 7(a). The EFD data matches with NPD profile within 3% error bound and almost identical wind profiles were observed among verifiers. The error to the prescribed NPD profile is satisfactory and less than 1% above 0.1 m where topside modules for FPSO are installed as in Fig. 7(b). The NPD wind profile used in this section was used for the wind load estimation of the semi-submersible rig and FPSO thereafter.

4.3. Semi-submersible rig

The target semi-submersible rig and associated surface mesh are as shown in Fig. 8. The hull is located in the center of domain as described in Fig. 5 and wind load calculation was conducted with sustainable wind profile shown in Fig. 6. Resulting mesh distributions following the volume mesh strategy described in section 3.3 are shown in Fig. 9.

Table 2
Results of grid sensitivity.

Mesh	Meshsize	Cx				Cy			
	[mil.]	180	E_r (%)	150	E_r (%)	150	E_r (%)	90	E_r (%)
coarse	10	−0.037	–	−0.045	–	0.049	–	0.121	–
medium	34	−0.033	−12.2	−0.038	−15.3	0.045	−7.3	0.107	−11.3
fine	58	−0.033	1.2	−0.040	4.6	0.043	−5.5	0.110	3.0
EFD		−0.036	–	0.048	–	0.048	–	0.112	
R		−0.089	–	−0.254	–	0.703	–	−0.233	–

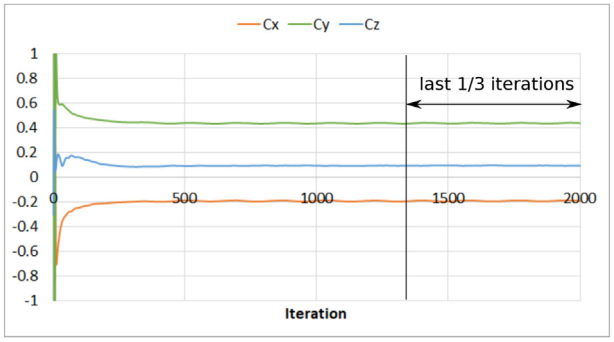

Fig. 6. Convergence history of wind load coefficients.

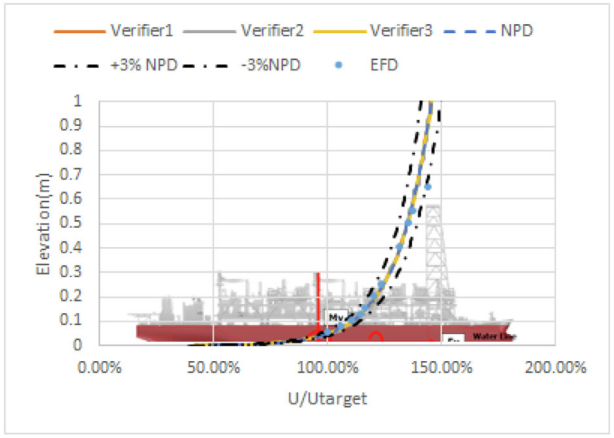

(a) NPD profile

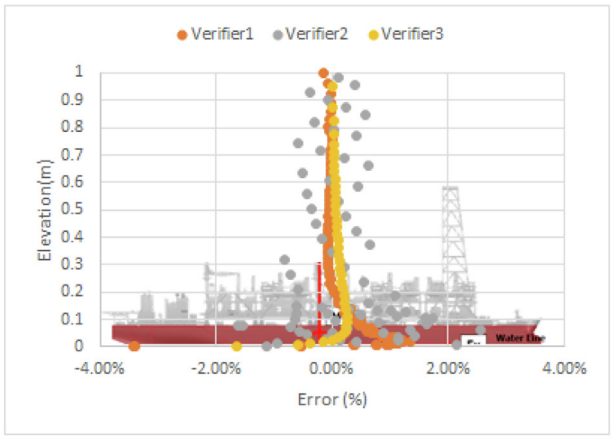

(b) Deviation between CFD solution and NPD profile

Fig. 7. Sustainable wind profile.

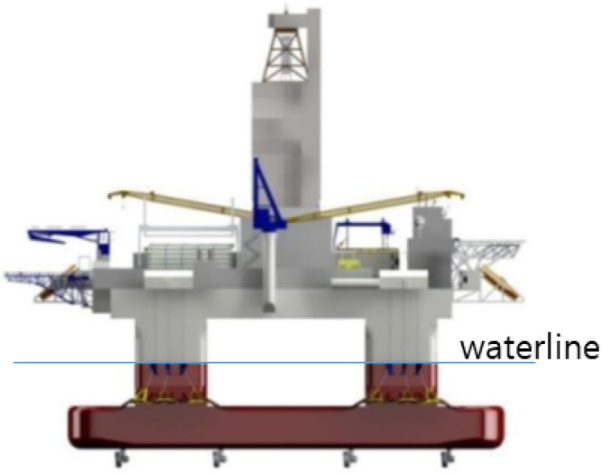

(a) geometry

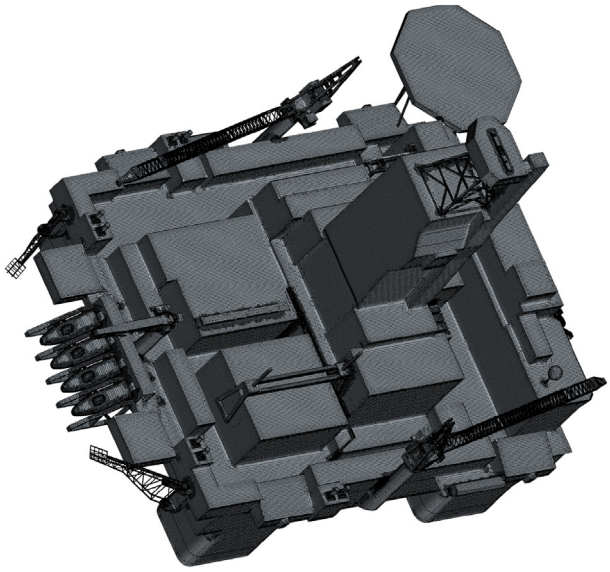

(b) surface mesh

Fig. 8. Semi-submersible rig.

The principal dimension of the semi-submersible rig is summarized in Table 3. Wind load calculation was conducted in model scale. It should be noted that since wind speed in model scale is determined in Reynolds dependency test considering wind tunnel capacity, the wind speed in model scale does not satisfy Reynolds similarity with wind speed in prototype. Even though the calculation was conducted in model scale, the wind load coefficients is applicable to the full-scale model since loads on blunt bodies with sharp edges are less sensitive to Reynolds number and the wind

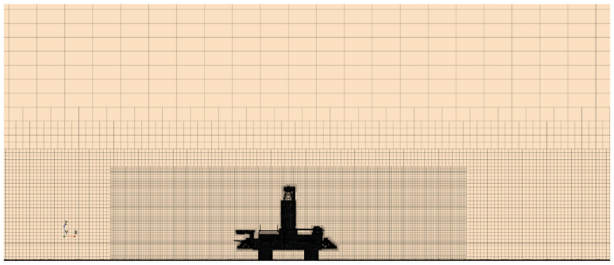

(a) side view

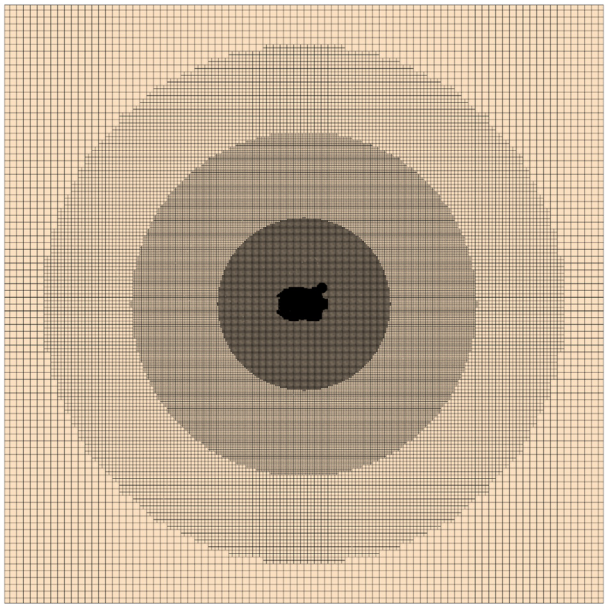

(b) top view

Fig. 9. Mesh distribution for semi-submersible rig.

Table 3
Principal dimension of semi-submersible rig.

	Prototype	Model
L_{pp} (m)	127.4	0.509 6
B (m)	86.1	0.344 4
H (m)	127.5	2.55
T (m)	25.2	0.100 8
U (m/s)	40	8.58
Re	3.0E8	3.0E5
λ	250	

speed for model scale was determined by the Reynolds number dependency test. The experiment was planned such that geometrical uncertainties were minimized and model was built with 3-D printer from 3-D CAD provided by Samsung Heavy Industries (SHI). All the verifiers were given the same 3-D CAD for the benchmark such that geometrical uncertainties between CFD and experiment were minimized.

Benchmark cases are summarized in Table 4. In addition to the even keel conditions which was conducted in TESK JDP (Yeon et al., 2019), inclined conditions in critical wind direction of 220° are considered. Even keel conditions consist of 12 heading angles from 0 to 360° with interval of 30°. Critical wind direction conditions consist of 20 cases which are made of 5 heading angles and 4 inclination angles.

For the even keel conditions, uncertainty levels between

Table 4
Test matrix for semi-submersible rig.

Condition	Headings [deg]	Draft [m]	Inclination [deg]
Evenkeel	0 to 360 (30° interval)	25.2	0
220 (Critial wind direction)	180 to 260 (20° interval)	25.2	5
		25.0	10
		24.9	17
		25.1	20

verifiers are evaluated with the following relation (Kim et al., 2018):

$$U_F = \frac{\text{std}(||F||)}{\text{avg}(||F||)} \qquad U_M = \frac{\text{std}(||M||)}{\text{avg}(||M||)} \tag{7}$$

where U_F and U_M are uncertainty in force and moment, std and avg are the standard deviation and average of the forces and moments from the simulations and $\|F\| = \sqrt{F_x^2 + F_y^2}$, $\|M\| = \sqrt{M_x^2 + M_y^2}$ where vertical forces and yaw moments are omitted since those values are so small by factor of 10 and above compared to other components and lateral drag and overturning moments are the principal forces and moments of interest for the semi-submersible rig design. It should be noted that the uncertainty contains both the uncertainty from two CFD softwares (Siemens STAR-CCM+ and OpenFOAM) and the uncertainty from meshes created within the range specified in the guideline of mesh strategy.

Uncertainty levels for each heading is summarized in Table 5. Uncertainty levels for forces are roughly around 6–8% and 2–5% for moments. Overall, uncertainty levels are not larger than 10% in any headings.

Fig. 11 shows wind load coefficients from verifiers with wind tunnel test results. It shows consistent results among verifiers and matches well with wind tunnel test within 10% error bound although some verifiers had a little deviated results than others. The strayed results compared to other verifiers were mainly related to the way of handling surface meshes of the complex geometries, particularly surface meshes with defects as shown in Fig. 10. Narrow gap between objects and small objects with sharp edges in Fig. 10(a) and 10(b) can lead to degenerate surface meshes which are apt to result in erroneous volume cells. For automatic mesh generator or top-down mesh generator like trimmer mesh or surface wrapper provided by Siemens STAR-CCM + or snappyHexMesh provided by OpenFOAM, those degenerate surface mesh generation could be avoidable by adjusting minimum surface mesh size at the cost of mesh size. Sometimes, feature line information including sharp edges are not properly preserved during mesh

Table 5
CFD results for semi-submersible rig among verifiers.

Heading	U_F	U_M
0	7.3%	2.1%
30	7.5%	1.6%
60	6.0%	2.7%
90	10.1%	4.0%
120	8.8%	4.5%
150	7.5%	3.1%
180	9.4%	7.1%
210	5.6%	1.8%
240	6.9%	0.6%
270	7.1%	2.5%
300	7.6%	1.4%
330	7.4%	2.7%

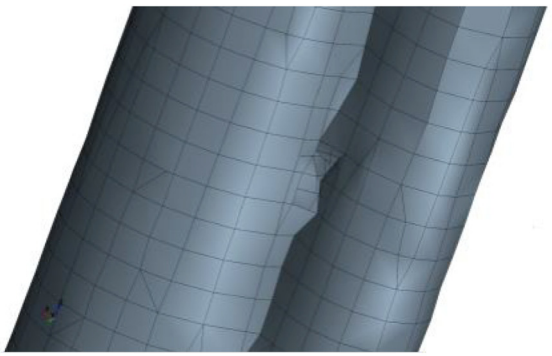

(a) narrow gap

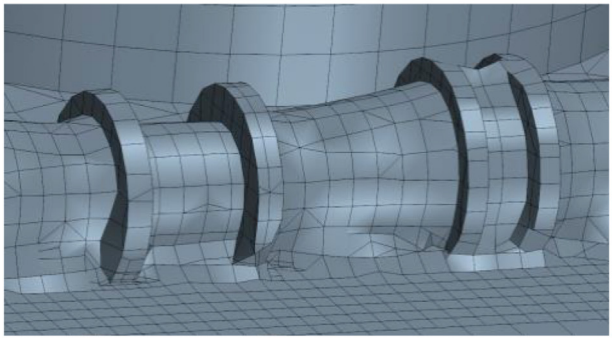

(b) small object with sharp edges

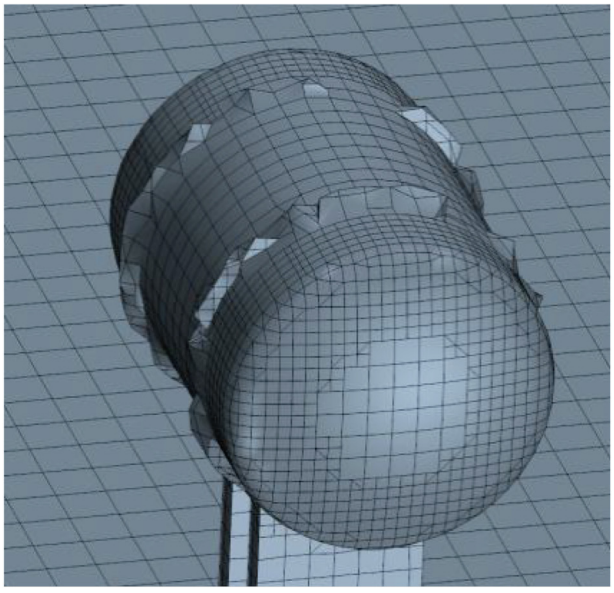

(c) crack on the surface

Fig. 10. Degenerate surface meshes.

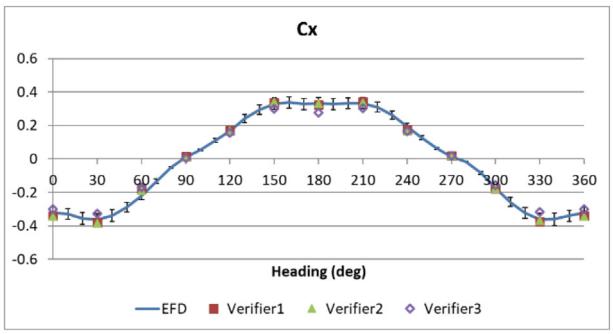

(a) Cx

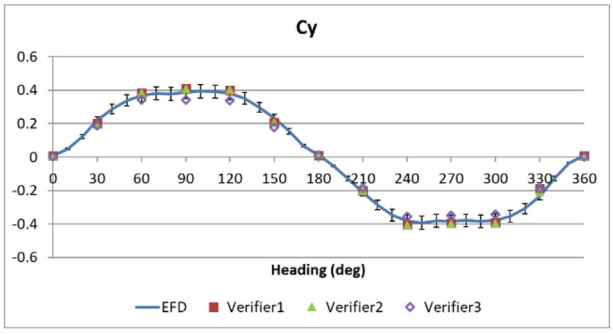

(b) Cy

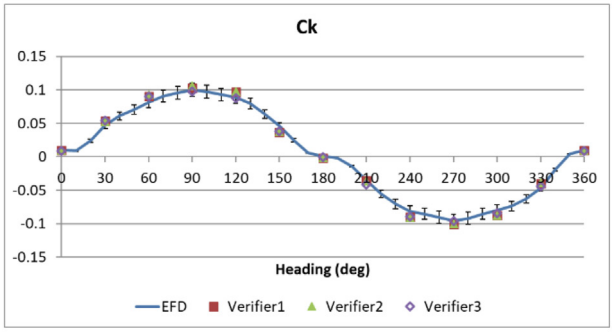

(c) Ck

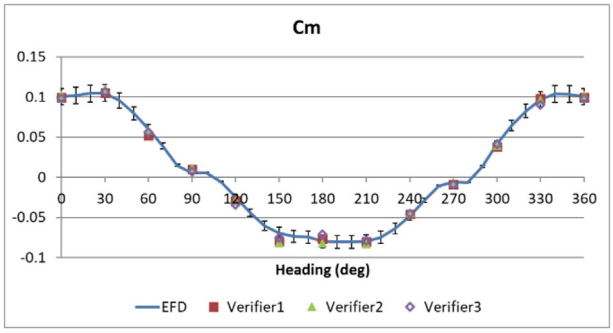

(d) Cm

Fig. 11. Wind Load Coefficients for even keel for semi-submersible rig.

generation process and lead to incorrect mesh. In that case, the feature line information should be regenerated or provided explicitly such that sharp corners are represented properly. The surface mesh can have incorrect topological information including zero face area, negative volume cell when dealing with geometries with cracks or non-watertight surfaces as shown in Fig. 10(c). The best way to prevent the erroneous behavior is to remove all the cracks on the surface before the mesh generation, which is often a bottle neck to the smooth CFD modeling because geometries referred to as dirty CAD are often provided in practice.

In addition to even keel conditions, uncertainties for inclined conditions are summarized in Table 6. For small angles below 10°, uncertainty levels are around 2–4% for forces and 3–6% for

Table 6
CFD results for semi-submersible rig among verifiers.

Heading	Incl. = 5deg		Incl. = 10deg		Incl. = 17deg		Incl. = 20deg	
	U_F (%)	U_M(%)	U_F (%)	U_M(%)	U_F (%)	U_M(%)	U_F (%)	U_M(%)
180	3.0	4.4	3.4	4.2	4.7	8.9	2.7	5.3
200	2.8	4.4	2.8	2.8	2.1	5.9	2.3	4.2
220	1.8	2.3	4.4	5.8	3.4	6.7	2.9	6.3
240	2.4	3.4	2.4	3.3	1.6	3.7	1.3	3.0
260	2.6	3.6	3.2	3.8	2.7	1.8	1.8	1.8

moments. Above 17°, uncertainty levels are around 2–4% for forces and 4–9% for moments with larger scatters than in small angles. Overall, uncertainty levels are not larger than 10% at any headings and inclination angles.

Fig. 12 shows wind load coefficients from verifiers with wind tunnel test results in inclination angle of 5° in critical wind direction of 220°. It shows wind load matched well with wind tunnel test within 10% error bound similar to the even keel case.

Fig. 13 shows wind load coefficients from verifiers with wind tunnel test results of inclination angle of 20° in critical wind direction of 220°. Overall, the consistent results were obtained and followed the wind tunnel test within 10% error bound. Larger deviations were observed in moment estimation, particularly at heading angle of 220°, which were not improved even with unsteady RANS simulation. Fig. 14 shows pressure distributions and streamlines on the bottom surface of the deckbox for the inclination angle of 5 and 20°, respectively. For the small inclination angle, A low pressure distribution is observed on the surface of the deckbox as the flows easily pass through the space below the deckbox without any obstruction as shown in Fig. 14(a). For the large inclination angle, it can be observed that the inclined deck box penetrates the floor and blocks the flow passing through the space below the deckbox, creating a stagnation point, resulting in a high pressure distribution as shown in Fig. 14(b).

Fig. 15 shows model configuration with inclination angle of 20° in critical wind direction of 220°. The columns of the model are installed through the turntable such that there are small gaps around the surfaces of the model, for instance, gaps around the deckbox and gaps around the columns. Since CFD simulations were conducted without considering those gaps, the existence of the gap may have effects on the pressure distribution, judging from the stagnation point shown in Fig. 14(b). Since the exact shape of the gap made in the wind tunnel test was not known, the size of the gap was assumed to be about 3 mm around the intersections of deckbox, columns and turntable and modelled with pressure outlet boundary conditions.

Fig. 16 shows the pressure distributions and streamlines of the topside surface with or without the gap. In the case with gap, the streamlines exhibit more complex structures in the wake of the hull and much reduced pressure distributions were observed on the topside surface as shown in Fig. 16(b). Owing to the gap, the pressure distributions on the columns were relaxed than in the case without gap as well. Fig. 17 shows the pressure distributions and streamlines of the bottom surface of the deckbox. High pressure distribution in the case where the gap was not considered is observed as shown in Fig. 17(a) which is a duplicate of Fig. 14(b) for easy comparison. The pressure distribution is relaxed under the deckbox and around the columns and the magnitude of the pressure is lowered in the case where the gap was considered as shown in Fig. 17(b) because the some parts of the flow could slip through the gaps. The averaged moment coefficients by the effect of the gap were summarized in Table 7. The moment coefficients C_k and C_m

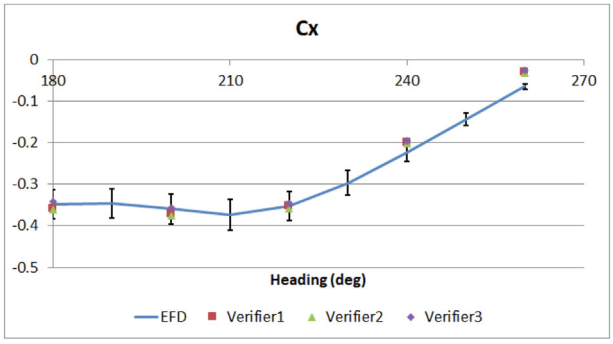

(a) Cx

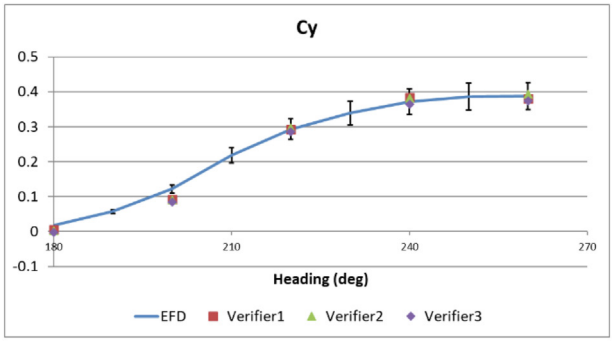

(b) Cy

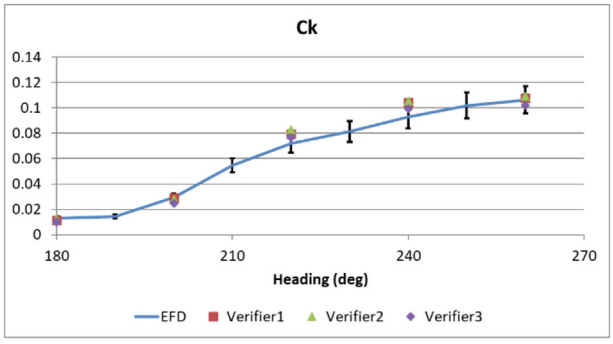

(c) Ck

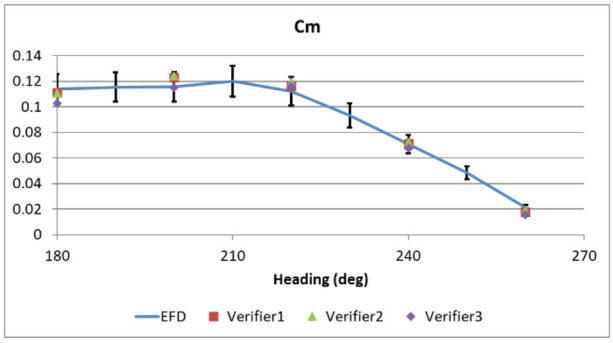

(d) Cm

Fig. 12. Inclination angle 5 deg. with critical wind direction 220 for semi-submersible rig.

were lowered and improved by 7.0% and 5.2% after applying the gap, respectively. Thus, it can be seen that the change of the moment was in part due to the change of the center of moments

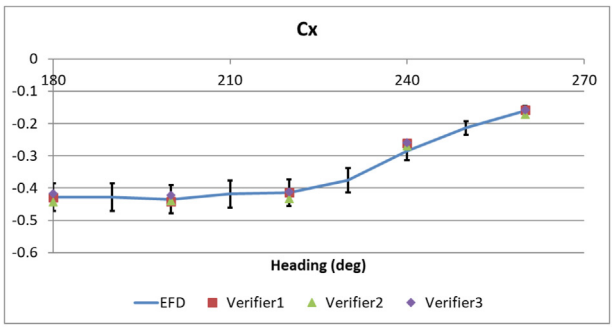

(a) Cx

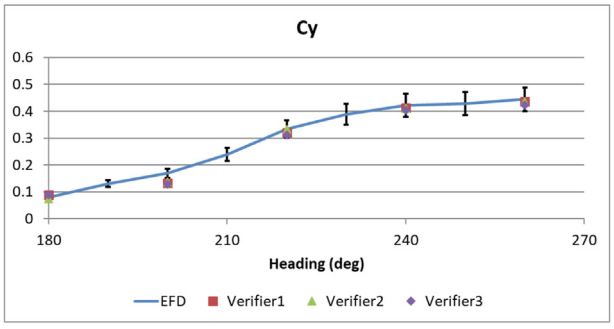

(b) Cy

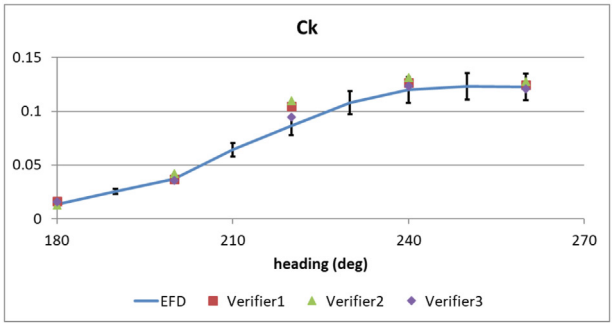

(c) Ck

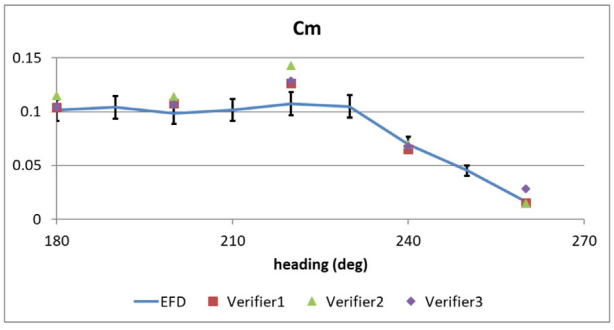

(d) Cm

Fig. 13. Inclination angle 20 deg. with critical wind direction 220 for semi-submersible rig.

resulted from the relieved pressure distributions on the bottom surface of the deckbox and the topside surface as well as the change of vertical force resulted from the balance of the pressure distributions on both the deckbox bottom and topside surfaces.

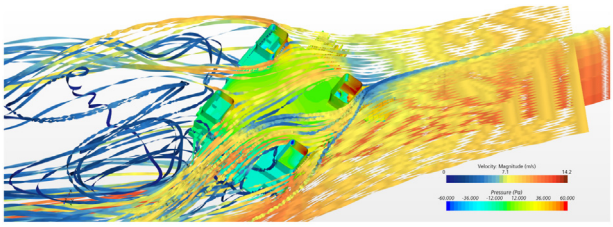

(a) inclination angle of 5 degrees

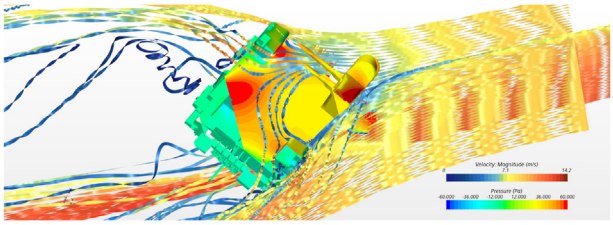

(b) inclination angle of 20 degrees

Fig. 14. Pressure distributions on the bottom surface of the deckbox in the critical wind direction of 220 degrees of semi-submersible rig.

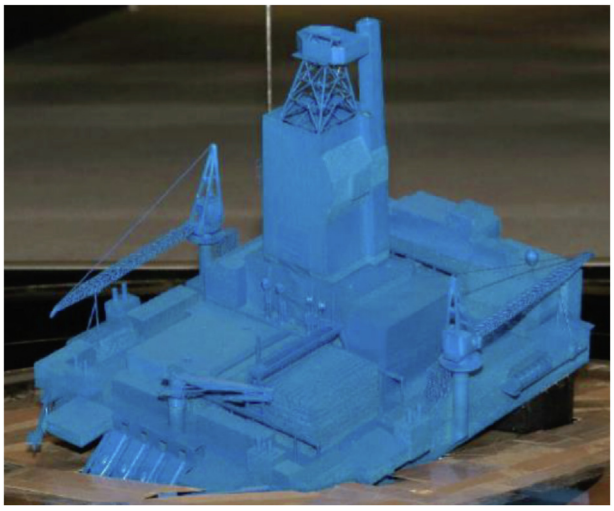

Fig. 15. Gaps between test model and turntable in wind tunnel configuration for semi-submersible rig.

However, since the shape and size of the gap was assumed without knowing it, a more in-depth case study on their influence might be needed in the future plans.

4.4. FPSO

The target FPSO and associated surface mesh are as shown in Fig. 18. The hull is located in the center of domain as described in Fig. 5 and wind load calculation was conducted with sustainable wind profile as well. Resulting mesh distributions following the volume mesh strategy described in section 3.3 are shown in Fig. 19.

Principal dimension of FPSO is summarized in Table 8. Wind load calculation was conducted in model scale. It should be noted that since wind speed in model scale is determined in Reynolds dependency test considering wind tunnel capacity, the wind speed in model scale does not satisfy Reynolds similarity with wind speed

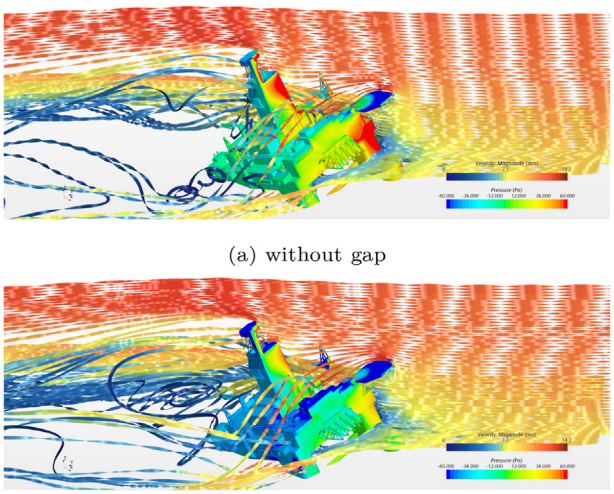

(a) without gap

(b) with gap

Fig. 16. Pressure distribution with streamlines on the topside surface of semi-submersible rig.

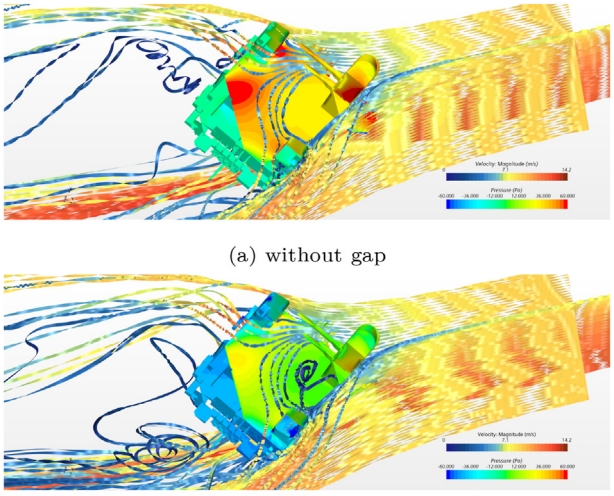

(a) without gap

(b) with gap

Fig. 17. Pressure distribution with streamlines on the bottom surface of semi-submersible rig.

Table 7
Results of gap effect of semi-submersible rig.

	C_k	C_m
without gap	0.106 (22.3%)	0.132 (22.6%)
with gap	0.099 (15.3%)	0.126 (17.4%)
EFD	0.087	0.108

in prototype. Even though the calculation was conducted in model scale, the wind load coefficients is applicable to the full-scale model since loads on blunt bodies with sharp edges are less sensitive to Reynolds number and the wind speed for model scale was

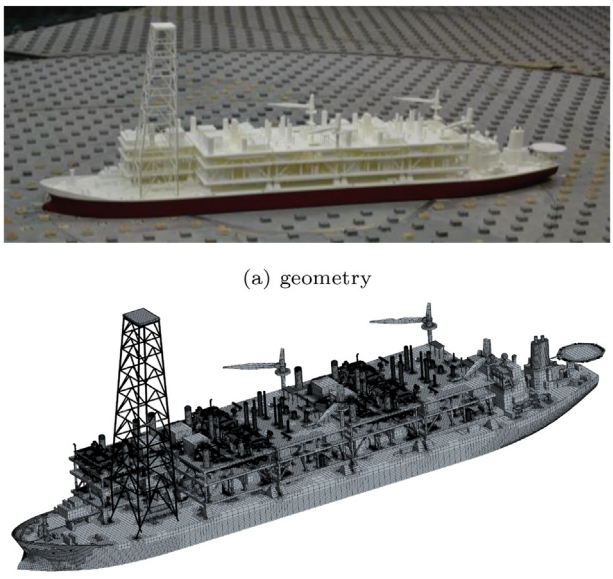

(a) geometry

(b) surface mesh

Fig. 18. FPSO.

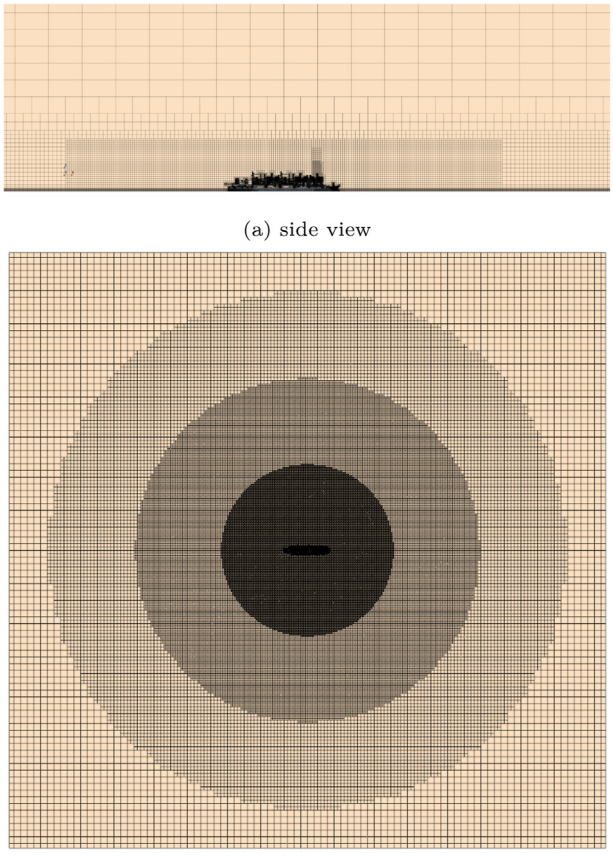

(a) side view

(b) top view

Fig. 19. Mesh distribution for FPSO.

Table 8
Principal dimension of FPSO.

	Prototype	Model
L_{pp} (m)	306.7	1.533 5
B (m)	58.8	0.294
H (m)	132.7	0.663 5
T (m)	16.0	0.08
U (m/s)	40	19.1
Re	8.0E8	2.0E6
λ	200	

Table 9
Test matrix for FPSO.

Condition	Headings [deg]	Draft [m]
Evenkeel	0 to 360 (30° interval)	16.0

Table 10
CFD results for FPSO among verifiers.

Heading	U_F (%)	U_M(%)
0	3.1	5.2
30	1.9	3.4
60	2.2	6.6
90	2.9	5.5
120	1.9	4.9
150	2.4	3.4
180	2.3	13.6
210	2.9	3.0
240	2.8	4.2
270	2.3	5.1
300	2.5	1.7
330	2.5	8.9

determined by the Reynolds number dependency test. The experiment was planned such that geometrical uncertainties were minimized and model was built with 3-D printer from 3-D CAD provided by SHI. All the verifiers were given the same 3-D CAD for the benchmark such that geometrical uncertainties between CFD and experiment were minimized.

Benchmark cases are summarized in Table 9. Even keel condition is considered. Even keel conditions consist of 12 headings angles from 0 to 360° with interval of 30°.

For the even keel conditions, uncertainty levels between verifiers are evaluated using Eq. (7) with $\|F\| = \sqrt{F_x^2 + F_y^2 + F_z^2}$, $\|M\| = \sqrt{M_x^2 + M_y^2 + M_z^2}$. Uncertainty level for each heading is summarized in Table 10. Uncertainty levels for forces are quite small, around 3%. For moments, larger scatter between 3–14% was observed.

Figs. 20 and 21 shows wind load coefficients from verifiers with wind tunnel test results. For FPSO wind tunnel test, a truncated model was used and there was a small gap (about 3 mm) between the water plane of the hull and the turntable of the wind tunnel. Since there is no gap at water line of FPSO in reality, CFD did not introduce any gap at the bottom boundary at the first try such that the effect from the gap was very clear in Fig. 20(c) and 21(a) and (b) for vertical degrees of freedom. The discrepancy which was already mentioned in Xu et al. (2019) without any detailed explanation can be explained with the pressure balance surrounding the hull.

Figs. 22 and 23 show the pressure distributions on the topside surfaces and bottom surfaces for the cases with or without gap

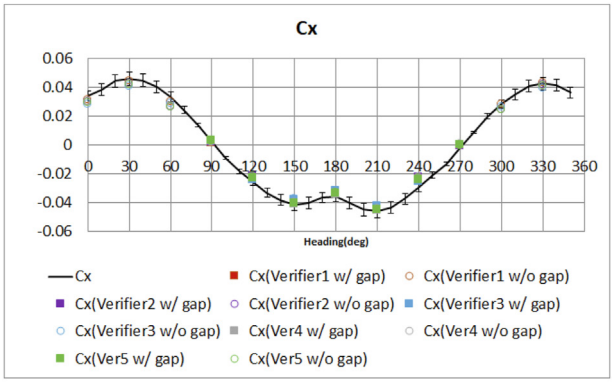

(a) Cx

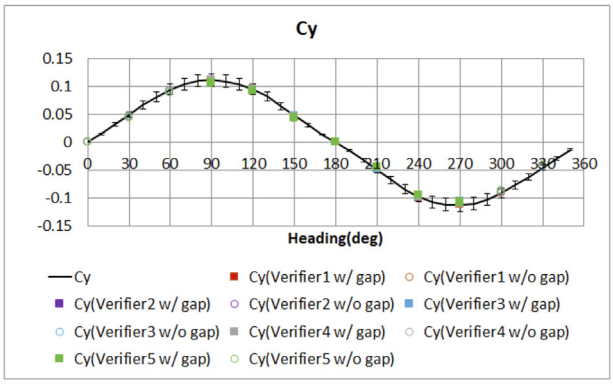

(b) Cy

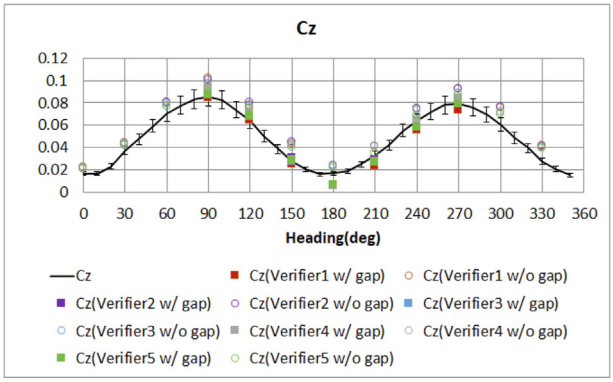

(c) Cz

Fig. 20. Wind load coefficient comparison between models with or without gap for FPSO (Forces).

between hull bottom and bottom boundary. As shown in Fig. 22, the pressure distributions on the topside surfaces are not discernible between the cases with or without gap. As shown in Fig. 23(a), the pressure distributions on the bottom surface are not involved in the pressure balance any longer for the case without the gap. For the case with the gap as shown in Fig. 23(b), hull surface in computational domain forms a closed volumetric surface such that the pressure on both top and bottom surfaces are balanced. As a result, much improved wind load coefficients could be obtained within 10% error bound by introducing the gap.

The vertical component of forces has some effects on moment evaluation as follows:

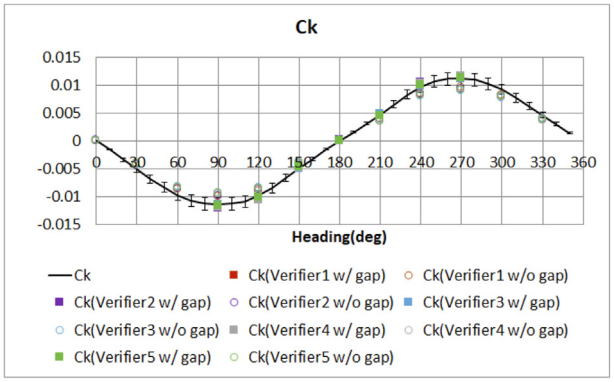

(a) Ck

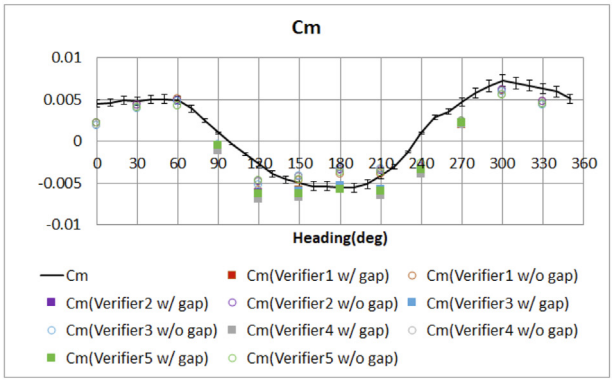

(b) Cm

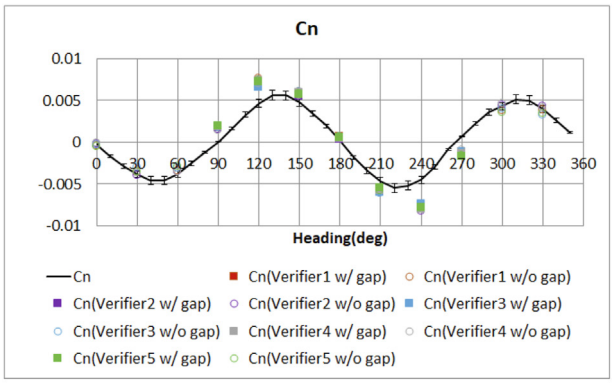

(c) Cn

Fig. 21. Wind load coefficient comparison between models with or without gap for FPSO (Moments).

$$\overrightarrow{\boldsymbol{M}} = \begin{bmatrix} M_x \\ M_y \\ M_z \end{bmatrix} = \sum \left(\overrightarrow{\boldsymbol{r}} \times \overrightarrow{\boldsymbol{F}} \right) = \sum \begin{bmatrix} F_y r_z - F_z r_y \\ F_z r_x - F_x r_z \\ F_x r_y - F_y r_x \end{bmatrix} \tag{8}$$

Roll and pitch moments can be influenced by introducing the gap and obtaining improved vertical forces. Particularly, roll moments show a better match with wind tunnel results, within 10% error bound. However, pitch moments show clear differences after introducing the gap but do not match well with wind tunnel results, particularly at 120 and 240° headings. In those headings, the estimated loads were within 50% error bound. Considering horizontal drag forces, C_x and C_y show an excellent match. Assuming

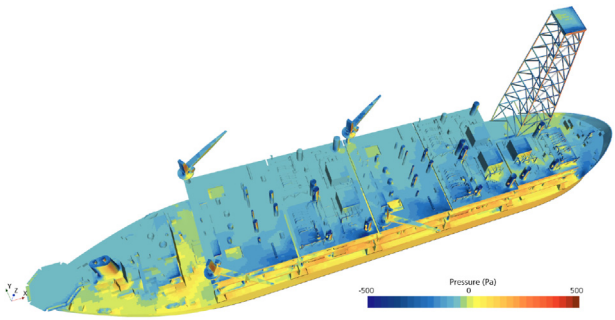

(a) without bottom gap

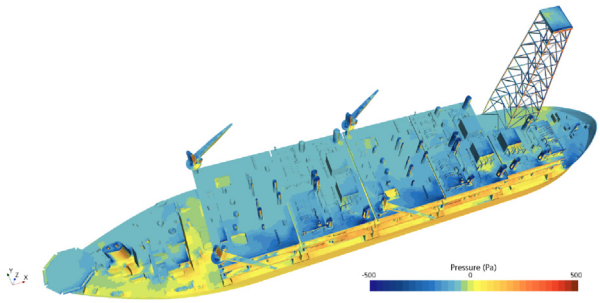

(b) with bottom gap

Fig. 22. Pressure distribution on the topside surface of FPSO.

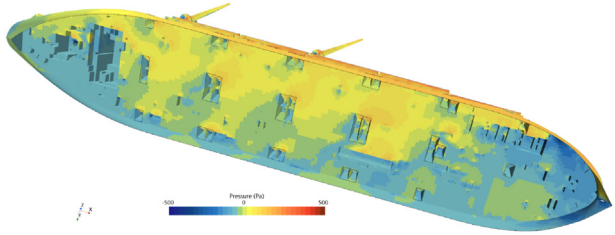

(a) without bottom gap

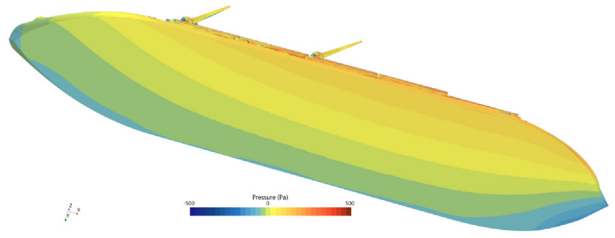

(b) with bottom gap

Fig. 23. Pressure distribution on the bottom surface of FPSO.

that lateral and vertical moment arms, r_y and r_z are comparable and much smaller than longitudinal moment arm, r_x, the uncertainty of longitudinal moment arm might lead to this discrepancy. In that sense, similar discrepancy observed in yaw moments shown in Fig. 21(c) could be explained. The main reason of the uncertainty is not clear at this stage. To resolve the issue, more scrutinized study should be made in terms of unsteady approach and turbulence model or surface roughness effect.

5. Conclusion

An overview of the developed modeling practice and the CFD results from verifiers in blind tests was provided. A sustainable wind profile modeling method was applied to compute wind load coefficients of offshore floating structures. The modeling practice was benchmarked against available model test results for a semi-submersible rig and an FPSO.

For the semi-submersible rig, an even keel and four inclined conditions were examined. The uncertainty levels between verifiers' results were about 6–8% for forces and 2–5% for moments in even keel condition and 3–5% for forces and moments in inclined condition. However, neither conditions showed uncertainty levels larger than 10%. For inclined conditions, as inclination angles increase, slightly larger scatters were observed but overall uncertainty levels are not larger than 10% at any heading and inclination angle. The discrepancy observed at heading angle of 220 were examined considering gap effect which existed in wind tunnel test but was not considered in the benchmark. After introducing the gap by assumption, the deviated values were improved but a more in-depth study is still needed for assessing the uncertainty observed in moment estimation clearly.

For the FPSO, an even keel condition was examined. The uncertainty levels between verifiers' results were quite small, around 3%, for forces. Relatively large scatters were observed for moments, especially at 120 and 240 headings. However, neither cases showed uncertainty levels larger than 14%.

Gap effect between hull bottom and turntable for the FPSO was studied. Owing to the differences of the pressure balance on the top and bottom surfaces of the hull, clear discrepancy was observed. Introducing a small gap between the bottom boundary and hull bottom in CFD led to better matches to wind tunnel test results. A large discrepancy still remained without further improvement at certain headings. For forces and roll moment, calculated wind loads were fit into 10% error bound. For pitch and yaw moments, large deviations especially at 120 and 240 headings were observed up to 50% error bound. Unsteady simulation might show better results at those headings but would be costly to calculate integral quantities like wind load coefficients from a practical point of view.

During the JIP work, it was found that CFD readiness for wind load estimation for offshore floating structures was quite high. A major bottleneck to smooth CFD modeling was geometry repair to make water-tight surface from CAD with many defects. In this regard, further work should be made for fast modeling approaches like voxel approximation or contouring methods including levelset, marching cube, dual contouring, to facilitate and ease the transition from CAD to CFD model.

Declaration of competing interest

The authors declare that they have no known competing financial interests or personal relationships that could have appeared to influence the work reported in this paper.

Acknowledgements

The authors thank Samsung Heavy Industries, TechnipFMC, Americal Bureau of Shipping, Bureau Veritas Solutions Marine & Offshore, Korea Shipping & Offshore Engineering, KRISO, and SINTEF Ocean for supporting this JIP and permission to publish this paper. The authors appreciate Samsung Heavy Industries for providing the model geometry data and model test reports for the semi-submersible rig and FPSO benchmark. The authors wish to acknowledge the important contributions of all the other individuals and JIP committee members involved in the JIP.

References

Achenbach, E., 1968. Distribution of local pressure and skin friction around a circular cylinder in cross-flow up to re= 5× 106. J. Fluid Mech. 34, 625–639.
Andersen, O.J., Løvseth, J., 2006. The Frøya database and maritime boundary layer wind description. Mar. Struct. 173–192.
API, 2000. Recommended Practice for Planning, Designing and Constructing Fixed Offshore Platforms–Working Stress Design. American Petroleum Institute.
Kim, J., Jang, H., Shen, Z., Yeon, S., 2019. Developing industry guidelines for the CFD-based evaluation of wind load on offshore floating facilities. In: Offshore Technology Conference. OnePetro, Houston, USA.
Kim, J., Jang, H., Xu, W., Shen, Z., Kara, M., Yeon, SeongMo, H, 2018. Numerical modeling of neutrally-stable and sustainable atmospheric boundary layer for the wind load estimation on an offshore platform. In: ASME 2018 37th International Conference on Ocean. Offshore & Arctic Engineering, Madrid, Spain p. V001T01A006.
Koop, A., Rossin, B., Vaz, G., 2012. Predicting wind loads on typical offshore vessels using CFD. In: ASME 31th International Conference on Ocean. Offshore and Arctic Engineering, Rio de Janeiro, Brazil, pp. 731–742.
OCIMF, 1994. Prediction of Wind and Current Loads on VLCCs. Oil Companies International Marine Forum London.
Richards, P., Hoxey, R., 1993. Appropriate boundary conditions for computational wind engineering models using the k-e turbulence model. J. Wind Eng. Ind. Aerod. 46, 145–153.
Richards, P.J., Norris, S.E., 2011. Appropriate boundary conditions for computational wind engineering models revisited. J. Wind Eng. Ind. Aerod. 257–266.
Roshko, A., 1961. Experiments on the flow past a circular cylinder at very high Reynolds number. J. Fluid Mech. 10, 345–356.
Sumner, J., Masson, C., 2010. kE simulations of the neutral ABL: achieving horizontal homogeneity on practical grids. In: 48th AIAA Aerospace Sciences Meeting Including the New Horizons Forum and Aerospace Exposition.
Weller, H.G., Tabor, G., Jasak, H., Fureby, C., 1998. A tensorial approach to computational continuum mechanics using object-oriented techniques. Comput. Phys. 12, 620–631.
Xing, T., Stern, F., 2010. Factors of safety for richardson extrapolation. J. Fluid Eng. 132.
Xu, W., Huang, Z., Kim, H., 2019. Thorough verification and validation of CFD prediction of FPSO wind load for confident applications. In: ASME 2019 38th International Conference on Ocean. Offshore and Arctic Engineering, Glasgow, Scotland, UK p. V001T01A001.
Yeon, S., Jang, H., Kim, J., Kim, J., Nam, B., Huang, Z., O'Sullivan, J., Kim, H., Hong, S., 2019. Numerical modeling practice and verification of the wind load estimation for FPSO and semi-submersible. In: ASME 2019 38th International Conference on Ocean. Offshore and Arctic Engineering, Glasgow, Scotland, UK p. V001T01A007.